

Relative Trajectories for Multi-Angular Earth Observation using Science Performance Optimization

Sreeja Nag
Massachusetts Institute of Technology,
Cambridge, MA 02139
Email: sreeja_n@mit.edu

Charles Gatebe
GESTAR/USRA
NASA GSFC, Greenbelt, MD 20771
Email: Charles.K.Gatebe@nasa.gov

Olivier de Weck
Massachusetts Institute of Technology,
Cambridge, MA 02139
Email: deweck@mit.edu

Abstract—Distributed Space Missions (DSMs) are gaining momentum in their application to earth science missions owing to their unique ability to increase observation sampling in spatial, spectral and temporal dimensions simultaneously. This paper identifies a gap in the *angular* sampling abilities of traditional monolithic spacecraft and proposes to address it using small satellite clusters in formation flight. The science performance metric for the angular dimension is explored using the Bidirectional Reflectance-distribution Function (BRDF), which describes the directional variation of reflectance of a surface element. Previous studies have proposed the use of clusters of nanosatellites in formation flight, each with a VNIR imaging spectrometer, to make multi-spectral reflectance measurements of a ground target, at different zenith and azimuthal angles simultaneously. In this paper, a tradespace of formation flight geometries will be explored in order to optimize or maximize angular spread and minimize BRDF estimation errors. The simulated formation flight solutions are applied to the following case studies: Snow albedo estimation in the Arctic and vegetation in the African savannas. Results will be compared to real data from previous airborne missions (NASA’s ARCTAS Campaign in 2008 and SAFARI Campaign in 2000).

1. INTRODUCTION

Distributed Space Missions (DSMs) are gaining momentum in their application to earth science missions owing to their ability to increase observation sampling in spatial, spectral, temporal and angular dimensions. DSMs include homogenous and heterogeneous constellations, autonomous formation flying clusters [1] and fractionated spacecraft [2]. To avoid being cost prohibitive, small satellites will be required to enable DSMs, especially those with large numbers. Small satellites have typically been used for technology demonstrations and educational programs [3],[4]. In this paper, we identify a critical Earth science application for DSMs, propose a coupled engineering and science model to evaluate the value of DSMs compared to monoliths and use the model to inform design choices for the DSM. The coupled model allows science variables such as estimation errors drive the engineering design choices of the DSM.

2. DISTRIBUTED SPACECRAFT FOR MULTI-ANGULAR OBSERVATION

In earth science remote sensing, distributed space missions or DSMs have been traditionally used to simultaneously improve sampling in the following four dimensions of an observed image – spatial, temporal, spectral, and radiometric. Spatial resolution of an image can be increased by using multiple satellites in formation flight to synthesise a long baseline aperture as shown for optical interferometry[5] and synthetic aperture radars. Constellations of evenly spaced satellites on repeat track orbits ensure temporal sampling within a few hours as well as continuous coverage maintenance. Spectral sampling can be improved by fractionating the payload (fractionated spacecraft) such that each physical entity images a different part of the spectrum and has customized optics to do so. Radiometric resolution depends on the resolution of the other sampling

TABLE OF CONTENTS

1. INTRODUCTION	1
2. DISTRIBUTED SPACECRAFT FOR MULTI-ANGULAR OBSERVATION	1
3. DATA AND METHODS	3
4. RESULTS AND INFERENCES	7
5. CONCLUSIONS.....	14
6. FUTURE WORK	14
7. ACKNOWLEDGEMENTS	15
REFERENCES.....	15
BIOGRAPHIES.....	17

dimensions for a fixed instrument mass and complexity. Since DSMs allow sampling improvement in any dimension by increasing satellite number instead of size, radiometric resolution can be improved without compromising on other science sampling requirements. Our research focuses on improving angular sampling, which is a critical dimension for Earth observations.

DSMs for Improved Angular Sampling

Angular sampling implies taking images of the same ground spot at multiple 3D angles of solar incidence and reflection simultaneously. A near-simultaneous measurement requirement deems monoliths insufficient for accurate and dense angular sampling [6][7]. Monolithic spacecraft have traditionally approximated the angular samples by combining measurements taken over time with forward-aft (e.g. TERRA’s MISR[8]) or cross-track swath (e.g. TERRA’s MODIS[9]) sensors. However, a single satellite can make measurements only along a restrictive plane with respect to the solar phase and most earth observation satellites are even more restricted since they are on sun-synchronous orbits. Further, the angular measurements are separated in time by many minutes along-track or weeks cross-track. In areas of fast changing surface/cloud conditions especially during the snow melt season/tropical storms, a few days can make a big difference in reflectance.

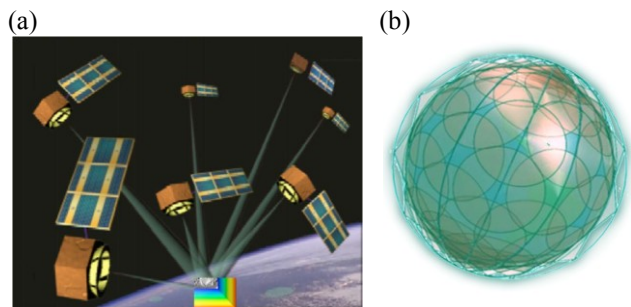


Figure 1: (a) A DSM making multi-angular, multi-spectral measurements by virtue of pointing its NFOVs at the same ground spot, as it orbits the Earth as a single system (adapted from Leonardo BRDF[10]). (b) A DSM making multi-angular, multi-spectral measurements by virtue of their overlapping WFOVs at different angles (from GEOScan[11]).

Near-simultaneous angular sampling can be improved by using a cluster or constellation of nanosatellites on a repeating-ground-track orbit[7]. The cluster can make multi-spectral measurements of a ground spot at multiple 3D angles at the same time as they pass overhead either

using narrow field of view (NFOV) instruments in controlled formation flight (Figure 1-a) or wide field of view (WFOV) instruments with overlapping ground spots imaged at different angles flight (Figure 1-b).

Previous studies have demonstrated the technical feasibility of subsystems [6], availability of formation flight strategies [7], [12], suitability of payload development [13] to support such a mission as well as open-source flight software to continually update satellite capability for staged, scalable deployment [3], [14]–[16]. This paper focuses on quantifying and presenting the science performance benefits derived from improved angular sampling of a formation flight DSM mission with NFOV sensors (Figure 1a).

Metrics for Angular Sampling

The widely accepted metric to quantify the angular dependence of remotely sensed signal is called BRDF or Bidirectional Reflectance-distribution function. BRDF of an optically thick body is a property of the surface material and its roughness. It is the ratio of reflected radiance to incident irradiance that depends on 3D geometry of incident and reflected elementary beams[17]. It depends on four major angles – the solar zenith and azimuth angle and the view zenith and azimuth angle. The azimuth angles are simplified to one angle called the relative azimuth angle. BRDF is used for the derivation of surface albedo[18], calculation of radiative forcing[19], land cover classification[20], cloud detection[10], atmospheric corrections, and aerosol optical properties[21]. BRDF estimations have proven to be good indicators of human activities e.g. ship wakes increase reflected sunlight by more than 100% [22].

Accurate BRDF time series at customized spectra and spatial scales can estimate many biophysical phenomena that are currently wrought with errors. For example, up to 90% of the errors in the computation of atmospheric radiative forcing, which is a key assessor of climate change, is attributed to the lack of good angular description of reflected solar flux[23]. MODIS albedo retrievals show errors up to 15% due to its angular and spatial under-sampling when compared to CAR. Gross Ecosystem Productivity (GEP) estimations, to quantify sinks for anthropogenic CO₂, show uncertainties up to 40% and usage of CHRIS angular data has shown to bring them down to 10%[24]. Accuracy of BRDF estimation is therefore a representative metric of the ‘goodness’ of angular sampling.

3. DATA AND METHODS

This paper will demonstrate equal or improved angular sampling performance characterized by BRDF using clusters in formation flight. A tightly coupled systems engineering and science evaluation model will be used for the purpose as shown in Figure 2.

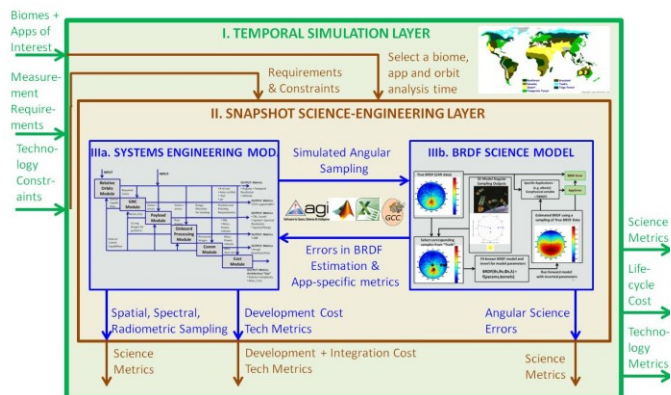


Figure 2: Summary of the overall approach to calculate BRDF science performance, technological requirements and cost of different mission architectures. There are three layers of analysis, this paper focuses on the inner brown and blue layers only.

The overall model has three layers. Box II (middle, brown layer) is responsible for simulating angular sampling from a tradespace of cluster designs and orbits via the systems engineering model (Box IIIa in blue) and evaluating the BRDF error term for each design via the BRDF science model (Box IIIb in blue) at any instant of time. The error term represents the difference between BRDF estimated using a simulated cluster compared to BRDF data from a heritage airborne instrument. The outer layer (Box I in green) is responsible for repeating this process over multiple orbits spanning the mission lifetime. The full system will take measurement requirements (e.g. angular and spatial sampling), technology constraints (e.g. maximum mass, highest altitude) and biomes of interest (e.g. vegetation, deserts) as input and produce three outputs: science metrics (e.g. BRDF error), lifecycle cost and extent to which technology constraints were met. Biomes are large naturally occurring communities of flora and fauna occupying major habitat. They have very different BRDF and therefore may need different cluster designs to capture their BRDF, hence prioritizing them is important to decide a global cluster design.

The model's utility is to find cluster designs that maximize science performance and minimize cost (outputs of Box I). This paper will concentrate *only* on the

innermost (blue Box III) layer, their mutual coupling and identify cluster designs based it. The BRDF science model will be discussed later in this section.

Data from Cloud Absorption Radiometer

One of the best examples for BRDF specific missions have been on the airborne side in the form of the Cloud Absorption Radiometer (CAR) instrument which was developed at NASA Goddard Space Flight Center (GSFC) [16] [20]. The CAR is designed to scan from 5° before zenith to 5° past nadir, corresponding to a total scan range of 190° . Each scan of the instrument lies across the line that defines the aircraft track and extends up to 95° on either side of the aircraft horizon. The CAR field of view (FOV) is 17.5 mrad (1°), the scan rate is 1.67 Hz, the data system has nine channels at 16 bits, and it has 382 pixels in each scan line. CAR's 14 bands are located between 335 and 2344 nm. The CAR is flown on an airborne platform (e.g. Convair CV-580 and C-131A), therefore by flying the instrument around a particular ground spot in circles and at different heights it is possible to get thousands of multi-angular and multi-spectral radiance measurements used for the accurate estimation of BRDF [25] [21].

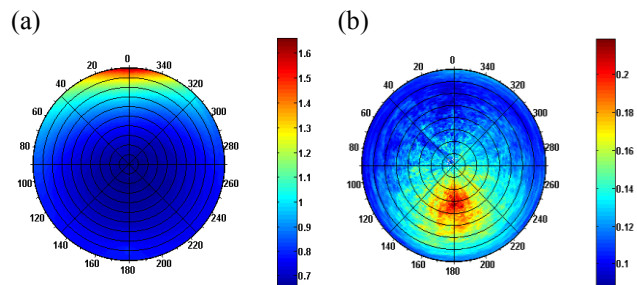


Figure 3: BRDF data collected by the Cloud Absorption Radiometer during two NASA airborne campaigns: ARCTAS in 2008 looking at Arctic snow (a) and SAFARI in 2000 looking at savannah vegetation (b) for wavelengths $1.03\mu\text{m}$ and $0.682\mu\text{m}$ respectively. Radius = view zenith angle, polar azimuth = relative azimuth angle. The Arctic location was Elson Lagoon (71.3°N , 156.4°W), Alaska and the savannah location 20.0°S , 23.6°E , Botswana.

The airborne measurements show very good correlation with laboratory estimations of BRDF using a goniometer setup [26]. Among its angular coverage over all view zenith and relative azimuth angles, CAR can sample BRDF in the principal plane (PP) i.e. the plane containing the sun and the normal from the target [27], which is very important for subpixel level vegetation structure and

other land remote sensing. Vegetation canopies often exhibit a pronounced peak called the hotspot on the PP and the amplitude and width of this feature is used to determine the biophysical parameters of the vegetation [28]. For this paper, the biomes of interest are selected to be Arctic snow and savannah vegetation. Both have very different BRDF signatures, are found at different geographic locations/latitudes and CAR data is available for both.

BRDF data for the arctic snow is available via NASA's ARCTAS campaign, which was conducted in 1–21 April 2008, with the aim of studying physical and chemical processes in the Arctic atmosphere and related surface phenomena, as part of the International Polar Year [18]. A site was selected 10 km east (upwind) of Barrow, Alaska, on Elson Lagoon. This lagoon is a protected arm of the Beaufort Sea. The surface consisted of flat land-fast first-year sea ice of thickness ~ 1.5 m, covered with 25–40 cm of snow with density 0.35 g cm^{-3} [18]. Data from CAR's channel 6 ($1.03 \mu\text{m}$) was chosen because clouds are most transparent to the near infra red band, eliminating the need for heavy atmospheric corrections for preliminary analysis. Reflectance at $1-90^\circ$ of view zenith angle and $1-360^\circ$ of relative azimuth angle with respect to the sun, collected by the CAR is plotted in Figure 3a where the solar zenith angle was 67° . The reflectance peaks at the sunglint when the view zenith angle is close to solar zenith, directly facing the sun. Snow albedo or black sky albedo is the integration of reflectance over all the view zenith and relative azimuth angles [18], [18], [27].

BRDF data for savannah vegetation is available via NASA's SAFARI campaign, where measurements were obtained during the Southern Africa Regional Science Initiative 2000 (SAFARI 2000) dry season campaign between 10 August and 18 September 2000 [21]. While reflectance measurements were collected at six locations in South Africa, Botswana, Namibia and Zambia, data from Maun in Botswana (20.00°S , 23.58°E) was selected for further analysis. Maun is located east of the Okavango Delta and has vegetation dominated by medium-sized multistemmed mopane trees. Solar zenith angle was 28° during winter. Data from CAR's channel 6 ($0.682 \mu\text{m}$) was chosen and plotted in Figure 3b. The green channel was chosen because it is the most relevant to photosynthetic efficiency which is a key application for estimating vegetation BRDF. BRDF is useful for correcting photosynthetic reflective indices (PRI) and estimate shadow fraction, which is then used to calculate

photosynthetic efficiency and therefore gross primary productivity [24], [29], [30].

Since the data used in this paper (Figure 3) is used as an example of true BRDF data and used to demonstrate the optimal ways to sample it, the age of the data is not of critical importance. It can be assumed that the approximate, average shape of BRDF of snow and savannah has not changed much in the last six to thirteen years, while the precise values of the function may have. Even so, since the CAR instrument and its campaigns are NASA's state-of-art in BRDF estimation, the available data is considered the best estimate of 'truth' for making engineering design choices.

BRDF Models

BRDF models are used to estimate reflectance values at all combinations of view zenith, solar zenith, and relative azimuth angle as a function of those angles and multiple parameters. These models may be classified in a number of ways [31]. One classification is based upon the treatment of the optics while another is classification as physical or empirical. Physical models rely upon first-principle physics of electromagnetic energy and material interactions, and require inputs such as surface roughness parameters and the complex index of refraction. Empirical models rely solely upon measured BRDF values, while semi-empirical models incorporate some measured data, but may have significant elements of physics-based principles. Models are dependent on the application, for example, computer graphics [32]–[34] or Earth observation [35]–[37].

For this study, we will concentrate only on semi-empirical models for earth observation. The most popular ones are the Ross-Li Thick-Sparse (RLTS) model [27], [38], Rahman-Pinty- Verstraete (RPV) model [39], [40], modified RPV to remove the non-linear terms in the RPV model and Cox-Munk model [22], [41]. RPV models have been applied for BRDF retrievals using MISR data while RLTS for MODIS data. For this paper, the RLTS model was selected because of its NASA heritage in generating BRDF products, proven merit in both snow [18] and vegetation [27] and linear form. BRDF by the RLTS model is given by the equations below and the kernels, K_{vol} and K_{geo} are graphed in Figure 4. Detailed discussion of the model is beyond the scope of this paper and can be found in several science-model focused literature [27], [38].

$$BRDF(\theta_s, \theta_v, \Delta\phi, \lambda) \cong R(\theta_s, \theta_v, \Delta\phi, \Lambda) \\ = f_{\text{ho}}(\Lambda) + f_{\text{vol}}(\Lambda)K_{\text{vol}}(\theta_s, \theta_v, \Delta\phi) \\ + f_{\text{geo}}(\Lambda)K_{\text{geo}}(\theta_s, \theta_v, \Delta\phi, P_4, P_5)$$

where:

$$K_{\text{vol}} = \frac{(\pi/2 - \xi) \cos \xi + \sin \xi}{\cos \theta_s + \cos \theta_v} - \frac{\pi}{4}$$

$$\cos \xi = \cos \theta_s \cos \theta_v + \sin \theta_s \sin \theta_v \cos \Delta\phi$$

$$K_{\text{geo}} = \frac{1 + \sec \theta'_s \sec \theta'_v + \tan \theta'_s \cos \Delta\phi}{2} \\ + \left[\frac{t - \sin t \cos t}{\pi} - 1 \right] (\sec \theta'_s + \sec \theta'_v)$$

$$\cos^2 t = \min \left\{ \left[\frac{P_4}{\sec \theta'_s + \sec \theta'_v} \right]^2 [D^2 + (\tan \theta'_s \tan \theta'_s \sin \Delta\phi)^2], 1 \right\}$$

$$\tan \theta'_x = P_5 \tan \theta_x; \quad x = v \text{ or } s$$

$$D = \sqrt{\tan^2 \theta'_s + \tan^2 \theta'_v - 2 \tan^2 \theta'_s \tan \theta'_v \cos \Delta\phi}$$

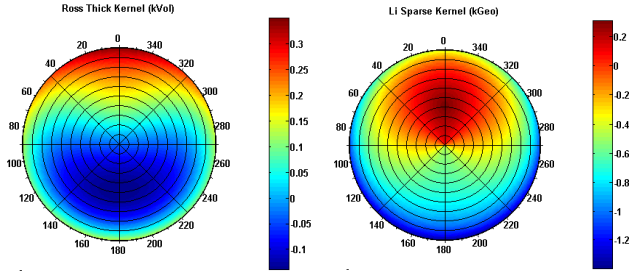


Figure 4: The two kernels of the RLTS model as a non-linear function of view zenith angle (plot radius) and relative azimuth angle to the sun (plot polar azimuth) at a solar zenith angle of 30° .

Formation Flight Models

Traditional and state-of-the-art frameworks are used to model the relative trajectories of the formation flight clusters so as to customize the angular spreads they are able to achieve. Previous studies [7], [12] have explored the tradespace of cluster designs in three levels of frameworks of increasing model fidelity and decreasing computational ease of exploration - Figure 5.

The first is the linearized Hill Clohessy Wiltshire Equations [42], [43] which we had to numerically correct to account for Earth's curvature at very large inter satellite distances. The HCW solution that gave the most angular diversity at the ground target was the Free Orbit Ellipse (FOE) configuration demonstrated in Figure 6(a) with 13 satellites, one always looking nadir. The cross-track scan (CTS) and string of pearls (SOP) solutions were achieved using the dual spiral equations [44] which

analytically accounts for the Earth's curvature, but does not produce as much azimuthal variation as the FOE. The second level is the modified HCW equations (curvature corrected) which introduces the effects of J2 perturbations due to the oblate shape of the Earth [45] and then atmospheric drag effects [46]. J2 and drag effects are simultaneously introduced by calculating a 7X7 state matrix and numerically solving it to compute relative satellite trajectories. Figure 6(b) shows the trajectories of 3 satellites in different colors with different ring sizes or maximum X-intercepts. The orange star is the ground target directly below the reference satellite (marked). The third and last framework of models uses AGI's Satellite Tool Kit to initialize and propagate individual satellite orbits (High Precision Orbital Propagator or HPOP) and then calculate their relative trajectories with respect to a reference satellite. SOP, CTS and FOE configurations of varying shapes, sizes and orientations can be created by varying the differential Keplerian elements of the satellite orbits [7], [12]. Previous studies have also mapped HCW coefficients to the differential Keplerian amounts for some special cases and orbits via the COWPOKE equations [47]. Figure 6(c) and (d) shows the relative trajectories of 3 satellites that form an FOE by varying their differential true anomaly, eccentricity and inclination (c) or RAAN (d). All (b)-(d) trajectories have been propagated for a day and it can be seen that drift due to differential inclination is more due to J2 effects.

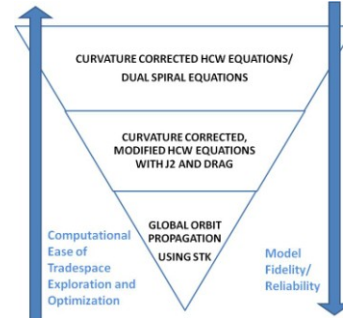
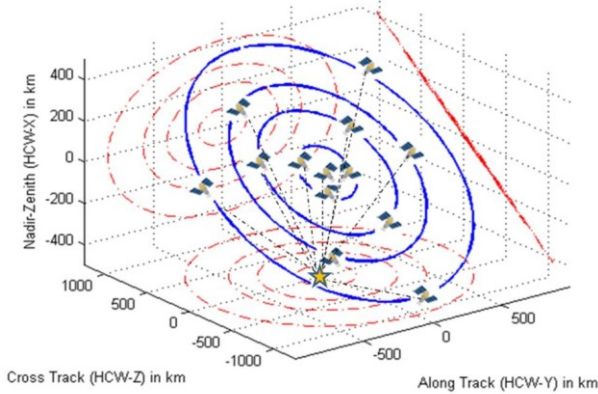


Figure 5: Levels of models used for formation flight simulation as a function of fidelity and computational ease of tradespace exploration.

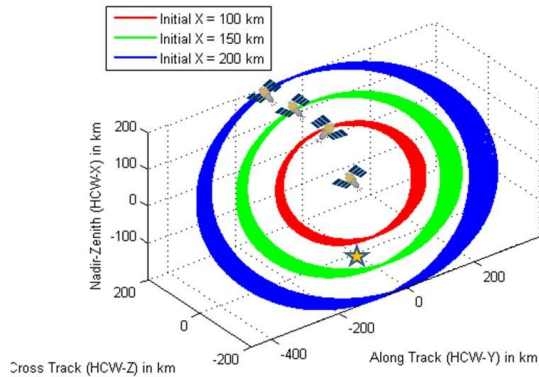
There are many free variables in all the frameworks (e.g. number of satellites, HCW coefficients) allowing us to vary them and get a wide variety of azimuthal and zenith angles subtended at the ground target point. External constraints like biome and latitude of interest determine the range of some variables. For example, differential inclination (RAAN) produces maximum separation at the poles (equator). FOE and CTS should be created by either one depending on target latitude where maximum angular spread is desired.

Figure 6: Trajectories of satellites in the Local-Vertical-Local-Horizontal (LVLH) frame as simulated using different levels of modeling from Figure 5. The orange star represents the point directly nadir to the reference satellite at [0, 0, -altitude] in the LVLH frame.

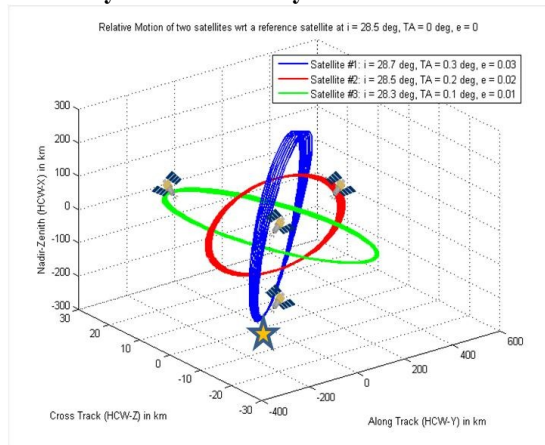
(a) Free Orbit Ellipse using the Hill Clohessy Wiltshire (HCW) Equations [42], [43] – 12+1 satellites



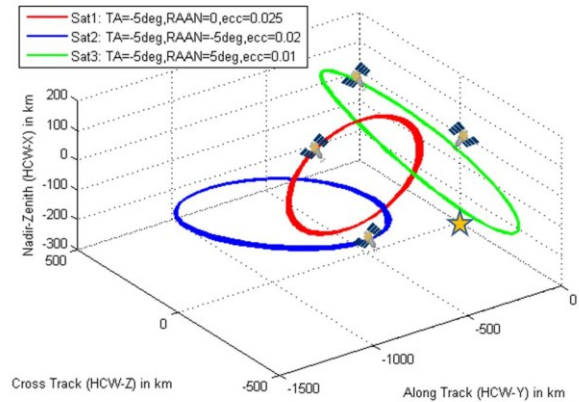
(b) Free Orbit Ellipse using the modified HCW Equations (with J2 and Drag effects) [45], [46] – 3+1 satellites



(c) Free Orbit Ellipse using HPOP Orbit propagation (STK) on 3+1 satellites with differential inclination, true anomaly and eccentricity



(d) Free Orbit Ellipse using HPOP Orbit propagation (STK) on 3+1 satellites with differential RAAN, true anomaly and eccentricity



Performance Evaluation Methods

Science performance in our model is computed in the Box IIIb (right blue box in the innermost layer) in Figure 2 and the detailed version is shown in Figure 7. The inputs to the Figure 7 model are the solar zenith, measurement zenith and relative azimuth angle of all satellites in a cluster at any given instant of time, which comes from the systems engineering model, and the biome of interest, which is an external requirement.

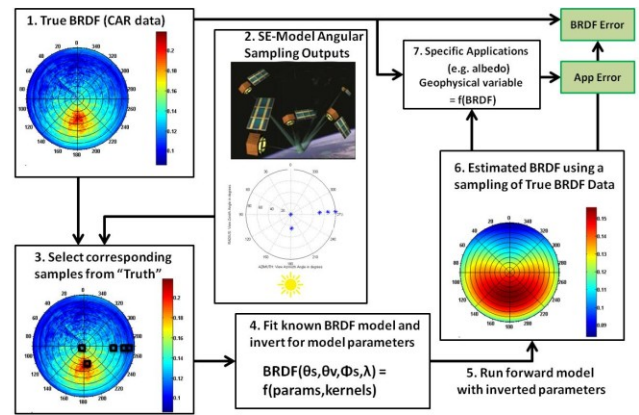


Figure 7: Summary of science performance evaluation (from the innermost blue box named ‘BRDF Science Model’ in Figure 2. The model combines angular output from the cluster architectures in the SE model with the BRDF science evaluation model. The metrics of performance are BRDF Error and Application Error, marked in green boxes.

True BRDF is the set of reflectance values of the biome of interest measured by CAR at all angles (e.g. Figure 3). A sample of these values that corresponds to the cluster angles is selected from the “True BRDF” and used as data

to invert a BRDF model (e.g. RLTS chosen) and estimate the model parameters. These parameters are then used to run the forward model and calculate reflectance at all angles. The difference between this estimated reflectance and the true CAR reflectance is called the “BRDF error” and is represented as a Root Mean Square value (RMS). BRDF can be used to calculate geophysical variables such as albedo and GPP. The difference between these variables calculated from the CAR reflectance values vs. from the forward model estimated values is called the “App Error”, e.g. albedo error. BRDF errors and App errors at any instant of time are the outputs from the science performance evaluation model and determine the goodness of the input cluster design and corresponding angular spread.

By calculating the error over time for a full tradespace of cluster architectures or designs helps us judge them based on an intricately coupled science metric. Eventually, these science based errors can be traded against the cost of increasing the number/size of satellites in and complexity of the DSM [48][49] and value-centric decisions for its engineering design [2].

4. RESULTS AND INFERENCES

The major drivers or influencers on BRDF errors that we wish to investigate are – The formation flight (FF) models and its internal variables to get a tradespace of angular spread [7], [12], biome type, geophysical parameters or supplication and temporal behavior of the cluster or constellation. In this section, we present four case studies where different FF models are plugged in with different biomes and parameters.

Linearized Frame and Snow Albedo

In the first case study, we plugged the Free Orbit Ellipse (FOE) configuration in the curvature corrected HCW frame to the science evaluation model for estimating snow BRDF and albedo. An FOE inclined at 21° with LVLH-X=0 plane was chosen based on previous studies that showed the possibility of large but consistent angular spread with such a configuration [7], [12]. A full tradespace enumeration of every possible way N satellites could orient on an FOE leads to tens of millions of architectures which is not efficient to explore because most of them are redundant and significantly underperforming. Since previous studies showed the necessity of a large angular spread, the satellites on the

FOE are forced into architectures with equal satellites per ring, equal azimuthal spacing in each ring and constrained to a maximum of 6 rings and 8 azimuthal slots. 5, 9 and 13 satellites were chosen for the study where 1 satellite was always forced to point nadir for reference reflectance measurements to benchmark the others against.

The results of the full factorial study are shown in Table 1 as the best and worst configuration for 5, 9, 13 satellites as judged by the BRDF error they produce with respect to the true CAR data in Figure 3a. The first column of figures shows the LVLH position of the satellites in FOE configuration at the instant of time which recorded minimum (top rows, best case) or maximum (bottom rows, worst case) errors. The second column shows the resultant measurement zenith and relative azimuth achieved by all satellites in each cluster by pointing their sensor to the ground spot directly below the LVLH origin (which always contains the reference satellite). Since global parameters are not considered in this frame of analysis, the sun is assumed to always be in the orbit plane of the reference satellite or the LVLH-Z=0 plane. In reality, the solar azimuth changes a lot causing the measurement azimuth to change a lot (unless the orbit is sun synchronous).

The worst errors are found when all the measurements are bunched up at near-nadir look angles i.e. negligible zenith range (red dots in second figure column). Errors are even worse when the measurement angles have no azimuthal spread and more so when they are asymmetrically concentrated on one side of the BRDF polar plot. For example, the worst case error with 5 satellites is more than an order of magnitude more than the worst case error with 9 satellites. Architecturally, this disparity was possible because the 6 ring maxima prevented 9 satellites from lining up on one side.

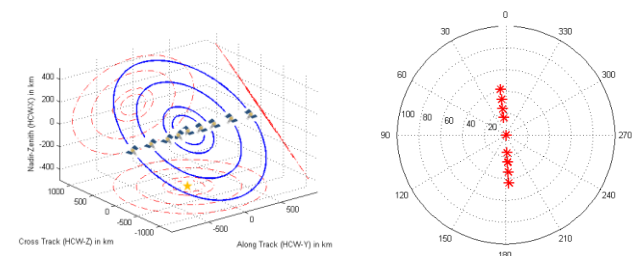
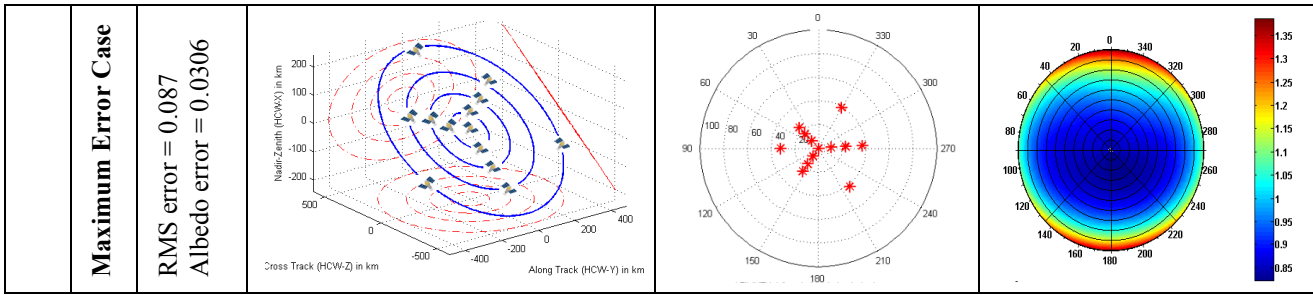


Figure 8: FOE configuration with 9 satellites with an RMS error of 0.087 with respect to true BRDF i.e. almost maximum error. This measurement configuration is very similar to that of MISR on the TERRA spacecraft with 9 sensors. However, it is very constrained in zenith angle range, which MISR is not.

Table 1: Results of the full factorial analysis of N satellites in an FOE configuration at 21° with X=0 plane, equally distributed in a flexible number of rings over equally spaced azimuth per ring. One satellite is always forced to point nadir as the reference satellite to make baseline reflectance measurements. In the BRDF polar plots, radius = view zenith angle, polar azimuth = relative azimuth with respect to the Sun.

			Cluster Configuration in the LVLH frame with trajectories from the HCW equations	Instantaneous Measurement Angles for the geometry shown	Estimated BRDF using parameters inverted on measurement samples shown
N = 5 satellites	Minimum Error Case	RMS error = 0.0582 Albedo error = 0.0059			
	Maximum Error Case	RMS error = 0.4884 Albedo error = 0.4			
N = 9 satellites	Minimum Error Case	RMS error = 0.0571 Albedo error = 0.0034			
	Maximum Error Case	RMS error = 0.0875 Albedo error = 0.03			
N = 13 satellites	Minimum Error Case	RMS error = 0.0570 Albedo error = 0.0024			



Errors almost the same as the maximum (<1% difference) in the $N = 9$ and 13 satellites case showed measurement angles line up in a straight line as seen in Figure 8. This configuration bears a strong resemblance to MISR's measurement spread except more constrained in the maximum zenith angle. MISR's BRDF error (calculated in the same way as Figure 7) is halfway between this maximum error and minimum error which translates to half an order of magnitude in albedo errors. This implies that having a large zenith range mitigates some error caused by the lack of azimuthal spread but cannot reduce it beyond a certain value. The least errors (blue dots in second figure column) for snow albedo and BRDF are always achieved by *both* zenith range (so that the sun glint at low sun conditions is captured) and azimuthal spread (so that the symmetry in the BRDF plot is captured). Large differences in look angles for identical satellites causes a huge elongation of swath, however this is a problem at MISR (with look angles varying from 0 to 70°) also has to deal with.

The best and worst BRDF RMS and albedo errors from the full factorial results in Table 1 are summarized as a function of the number of satellites in Figure 9. are summarized as a function of the number of satellites. Worst case errors drop significantly from 5 to 9 satellites, as explained by the fact that all 4 satellites bunched up in the same direction from the Sun which 9 and 13 satellites could not do. The worst case error drop between 9 to 13 satellites and the overall best case error drop is <0.3%, indicating nearly no gain in increasing satellite numbers. Since BRDF error is the sum of sampling goodness error, model error and model inversion error and the RLTS model is not a 'perfect' representation of earth reflectance (only 3 parameters), it may not be sufficient to capture the improving errors due to increasing spread because of its own coarseness. Since the inversion error is <0.5% or negligible, assuming a perfect model meant that almost entire error is a metric of sampling goodness. Availability of new spreads creates a scientific incentive to create better models such as those in computer graphics [32],

[33] or compressed imaging which uses a spherical harmonics representation of reflectance [50].

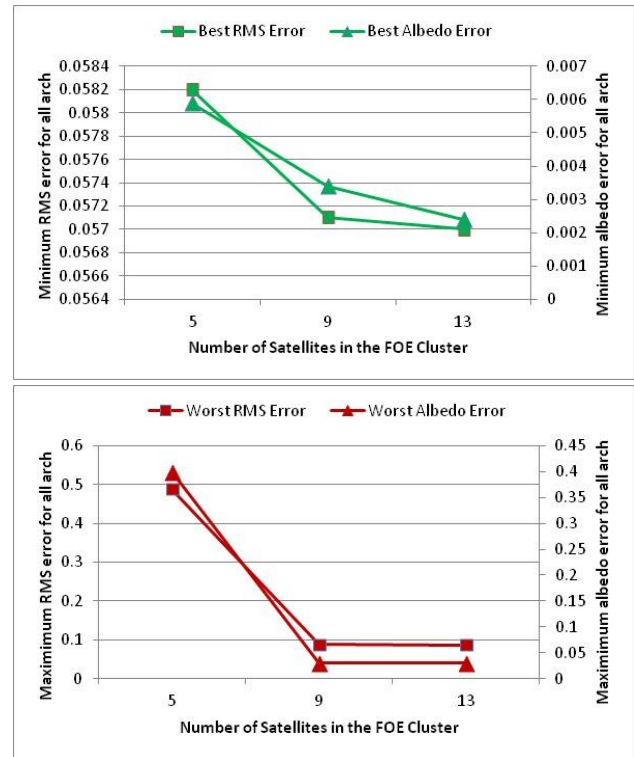


Figure 9: BRDF RMS error (left axis) and albedo error (right axis) with respect to CAR data for the best (green, top) and worst (red, bottom) configurations as a function of number of satellites in the informed full factorial simulation in Table 1.

Comparing the worst configurations for 9, 13 satellites and best configurations for 5, 9, 13 satellites also reveals ~40% difference in BRDF errors but very little absolute improvement. On the other hand, the worst case improvement from 5 satellites is 400%. This shows that if satellites are uniformly spread out in rings/zenith and azimuth as the full factorial study was forced to do (except in the 5 satellite case), we have leeway where even the worst is only ~0.001 worse than the best in albedo. This inference is important because the satellites

will spin around in the ellipse and the best configuration will distort periodically [7], [12] but can never get worse than the worst due to orbital dynamics alone, no perturbations considered.

Modified Linearized Frame and Snow Albedo

In the second case study, we plugged the modified HCW equation solutions, with J2 and atmospheric drag included and curvature corrected, to the science evaluation model for estimating snow BRDF and albedo [51]. To draw from the first case study, the number of satellites and HCW initial parameters were set in order to re-create the best configuration with 13 satellites (Table 1 5th row in this high fidelity frame. The trajectories were propagated for 15 orbits (~1 day) and shown in Figure 10-top. Six satellites each spin around the inner (red) and outer (blue) ring at equal spacing. Drag and J2 causes the rings to tumble about the cross axis as well as drift along track. The view zenith angle subtended at the ground target (orange star) by the first satellite on each ring is plotted in Figure 10-bottom. A small increase the angle subtended (trending at $\sim 2^\circ$) is seen over 15 orbits. The drift is characteristic of that seen in Figure 6(c) indicating a close analogy with the differential inclination driven FOE. Arctic snow sampling needs maximum angular spread and coverage at the poles, hence differential inclination (not RAAN) will be needed.

This calculation and plot assumes that the cluster always flies over snow for an entire day which is not realistic. However, the exercise is useful to evaluate the effect of error over time and inform decisions to phase the satellites so that the configuration when it flies over snow corresponds to minimum error.

When the angular spread achieved by the above cluster is plugged into the science evaluation model for snow BRDF, RMS errors can be calculated for each instant of time and plotted over 1-15 orbits. Figure 11 shows a small linear trend downward because of the slight increase in zenith angles subtended at the ground target which increases the closeness to sampling the sun glint. Too much drift would cause the formation to go over the horizon with respect to the reference satellite which would kill the simultaneous sampling capability of the cluster. Cluster maintenance strategies such as changing the reference satellite and/or commanding the other satellites to point at the ground track of the reference satellite instead of directly below it (assuming a few minutes time separation in making measurements is acceptable) and/or active propulsion can be adopted to

recover angular sampling capabilities in the event of too much drift.

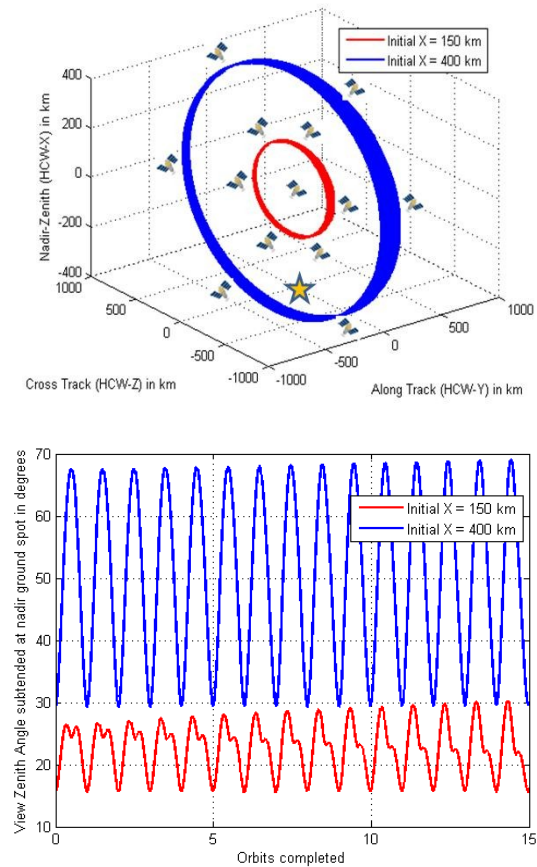


Figure 10: [Top] The best 13 satellite cluster configuration in Table 1 propagated over 1 day including J2 and atmospheric drag effects; trajectories of the inner (red) and outer (blue) ring shown in LVLH frame. Orange star represents the ground target at (0,0,-altitude) in LVLH frame. [Bottom] View zenith angle subtended at ground target for one satellite in the inner (red) and outer (ring). The graphs for the other 10 satellites are phase shifted versions.

Figure 11 also shows a distinct oscillatory pattern of the BRDF RMS errors with 6 oscillations per orbit (short term) and 1 oscillation per orbit (long term). The insets in Figure 11 show the measurement angles corresponding to select crests and troughs. The present of 6 satellites per ring ensures a wide azimuthal coverage and taps into the different quarters of the BRDF polar plot in spite of the orbital dynamics causing the satellites to rotate about the center. The patterns seem to indicate that crests correspond to maximum sampling along principal plane (0-180 line/plane, contains the sun) while the troughs correspond to the times when the satellites have all

rotated out of the principal plane. If the cluster is expected to encounter snow in X% of its orbit, we should phase the satellites such that the first or last X% of the orbit (least error) seen in Figure 11 corresponds to the flight over snow.

Figure 11's insets show the advantage that clusters with equally spaced satellites (in azimuth) have on sampling specific angles. The measurement spread remains almost the same over orbits because as one satellite rotates out of a given view zenith and relative azimuth angle, another one moves in to fill its space. Thus, if the cluster is designed such that some combination of angles is captured, equal azimuths will ensure that they are always captured – with more efficiency as number of satellites increases. This is all the more useful when changing solar azimuth angles are taken into account because the satellites rotate even faster because of it. Drift does cause some degradation in the view zenith angle and we discussed mitigation earlier in this section. Sun and drift caused dynamics are best assessed in the global STK frame, which is the highest level of frameworks we use.

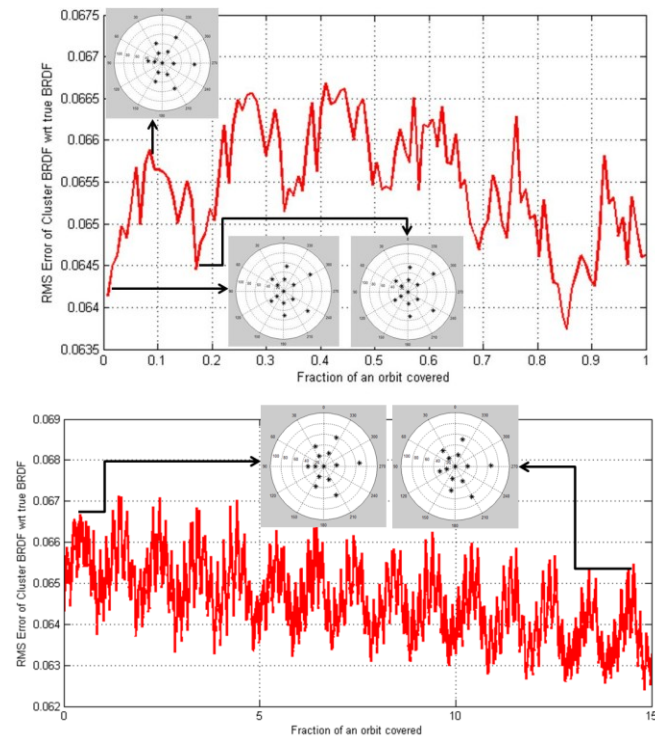


Figure 11: BRDF RMS error with respect to the CAR data for the cluster shown in Figure 10 when propagated for 1 orbit (top) and 15 orbits (bottom). Insets show the measurement angles achieved at specific points in time marked.

Snow BRDF vs. Vegetation BRDF

In the third case study, we plugged the Free Orbit Ellipse (FOE) configuration in the curvature corrected HCW frame to the science evaluation model for estimating vegetation BRDF in Southern Africa [51]. The study is essentially the same as the first case study except for a very different biome, with the intent of understanding the difference between the results caused by changing biomes. A full factorial analysis is done with the same variables and constraints as the first case study. Results are presented in Figure 12 for best (blue, left) and worst (red, right) error configurations using 4, 5, 9 and 13 satellites. The respective errors are noted on the first column as $e = [\text{minimum RMS error, maximum RMS error}]$. Figure 13 shows the dependence of these errors on the number of satellites.

As earlier, the worst errors occur when all the satellites are bunched toward near nadir i.e. $N = 4$ or 5 satellites, second (red) column in Figure 12. These configurations fail to capture the azimuthal variation of BRDF and, more importantly, the hotspot as seen in Figure 3b which is the peak reflection on the principal plane that occurs at view zenith angle equal to solar zenith angle with the sun behind the sensors. Worst case errors show a big drop between 5 to 9 satellites since the 9 satellites are forced to symmetrically arrange themselves on either side of nadir. While the worst case still occurs due to lack of azimuthal coverage, errors are improved because of the ability to capture the hotspot. Note the similarity to MISR's configuration except at much restricted zenith range, as before. The worst case in 13 satellites captures the full zenith variation of BRDF but not the hotspot at all, hence only a slight improvement in errors (red curve in Figure 13). The best case errors are seen (blue dots in Figure 12) when at least a part of the hotspot is captured, measurements are made in the upper hemisphere to capture the anti-hotspot *and* the zenith variation of BRDF is sampled.

The best case error for one time instant does not seem to depend on the number of satellites at all (green curve in Figure 13). For example, the best configuration in the 4 and 5 satellite case exploit the symmetry of the left and right hemisphere and achieve the same errors as the 9, 13 satellites with full zenith and azimuthal spread. However, the propagated over the whole orbit, the latter will do much better because the azimuthal sampling will compensate for the cluster rotating about the nadir. The 4 satellite case will be demonstrated in the STK frame to

show its drawback over time. The saturation could also be attributed to model errors, and spherical harmonics models will be tested instead of RLTS to assess the difference.

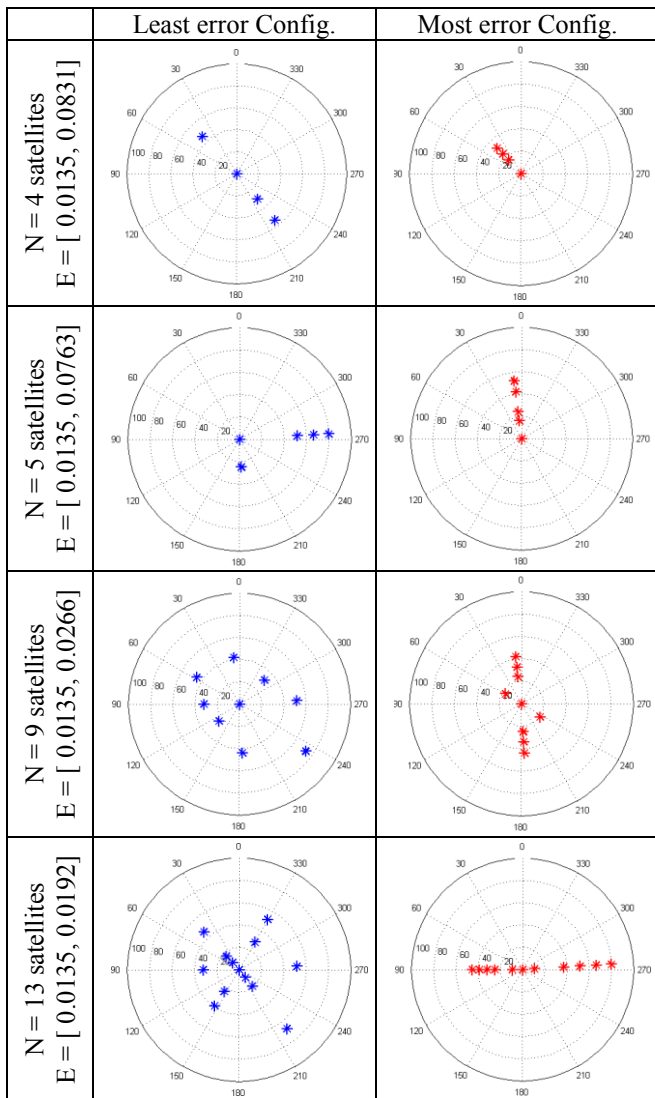


Figure 12: Measurement angles obtained with clusters with increasing number of satellites (rows) that gave the minimum (blue, column 1) and maximum (red, column 2) RMS error with respect to true BRDF of savannah vegetation measured by CAR, where $E = [\text{min Error, max Error}]$. In the polar plots, radius = view zenith angle, polar azimuth = relative azimuth with respect to the Sun.

The vegetation results are not extremely different from the snow results except a critical one: Snow needs more azimuthal sampling than vegetation. Vegetation produces the same and least error with a straight line sampling across the BRDF polar plot (N=4 satellites, blue dots in Figure 12) snow produces near maximum and never minimum errors in such a configuration (N=9 satellites,

red dots in Figure 8). Vegetation errors shoot up when the sampling is not available for top *and* bottom hemispheres. This difference explains why the MISR sensor which its 9 forward aft sensors does much better for vegetation than for snow. These results also agree very closely with an simulated annealing and genetic algorithm optimization to find the best and worst sampling points for vegetation and snow for 5, 9, 13 satellites.

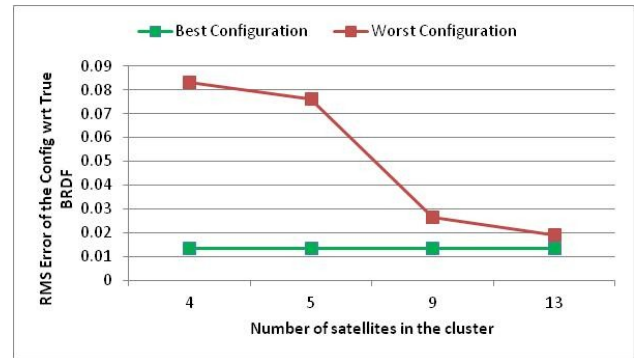


Figure 13: BRDF RMS error with respect to CAR data for the best (green) and worst (red) configurations as a function of number of satellites in the informed full factorial simulation in Figure 12.

Global STK Framework and Vegetation

In the fourth and final case study, we plugged the differential Keplerian element propagation in the global orbits frame (using AGI STK) to the science evaluation model for estimating vegetation BRDF as the cluster flies over Southern Africa [51]. The study requirements were considered in concurrence with current launch and funding opportunities: 4 satellites in a cluster with at least 1 nadir pointing satellite that are launched into a typical orbit using commonly available secondary launches. Individual spacecrafts are assumed to be 6U cubesats with no propulsion module on board. Requirements govern the flexibility in varying the differential Keplerian elements for the cluster satellites with respect to the reference satellite. The reference orbit was chosen at a 650 km altitude at 51.6° inclination to correspond to typical launch availabilities at near ISS orientations. Semi major axis (SMA) has to be the same for all satellites to prevent the formation from breaking. Lack of onboard propulsion restricts the variation of inclination, perigee and eccentricity because the cluster orbits cannot be initialized without propulsion. Differential inclination will also cause a tumbling effect which coupled with drift will eventually break the formation in the absence of active maintenance as seen in Figure 6(c). Therefore, the only free variables available are differential true anomaly (TA)

and differential RAAN (Ω). Differential variation of TA and RAAN cause a cross-track scan (in HCW frame) pattern which is more limited in azimuthal coverage than the FOE configuration.

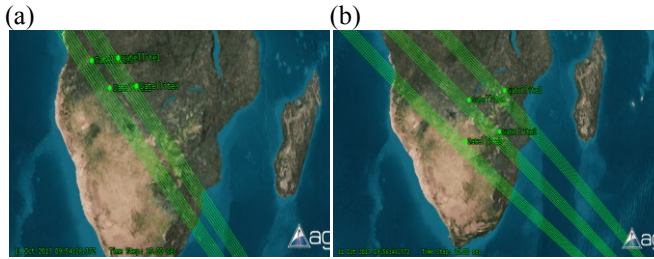


Figure 14: AGI-STK Astrogator propagated image of the satellite cluster as Config #6 (a) and Config #3 (b) as they fly over Southern Africa.

The very reduced full factorial analysis comprised of 6 cluster configurations where 4 of the 6 orbital elements were the same across all satellites: SMA = 6378+650 km, $i = 51.6^\circ$, $\omega = 0$, $e = 0$, and the RAAN and TA were perturbed by small amounts as listed in Table 2. Two of the configurations have been shown in an Astrogator propagated STK image as they fly over Southern Africa.

Table 2: RAAN and TA in the form of osculating Keplerian elements for 4 satellites in the cluster when arranged in different 6 configurations as part of a reduced full factorial case study. The other Keplerian elements are the same for all satellites, SMA = 6378+650 km, $i = 51.6^\circ$, $\omega = 0$, $e = 0$.

	RAAN::TA of the foll. satellites in degrees			
	Sat #1	Sat #2	Sat #3	Sat #4
Config #1	0::0	0::-5	-5::0	-5::-5
Config #2	0::0	0::-5	-5::0	5::-5
Config #3	0::0	0::-5	-5::-5	5::-5
Config #4	0::0	0::-5	-5::-3	5::-5
Config #5	0::0	0::-5	-5::-3	3::-3
Config #6	0::0	0::-3	-3::0	-3::-3

All clusters (using their initial osculating elements) and the MISR sensor (using TLEs from an online database) were simulated on STK starting October 13, 2013. A 20-minute time window when the cluster flies over southern Africa was identified on the same when the solar zenith angle is $\sim 30^\circ$, to match with the true CAR data available for Savannah vegetation (Figure 3b). MISR’s Africa-crossing time window is less than an hour ahead of the cluster’s time window. For each cluster and for each time instant over 20 minutes, the RMS error between the BRDF estimated by the cluster using Figure 7’s

methodology and true BRDF is calculated and plotted in Figure 15 as different colors. All of vegetated Africa is assumed to possess the BRDF signature shown in Figure 3b. True solar azimuth angle variation is considered and used to calculate relative azimuth angles. The same is repeated for MISR and plotted as black asterisks. Config #6 shows the highest RMS error and Config #3 the least.

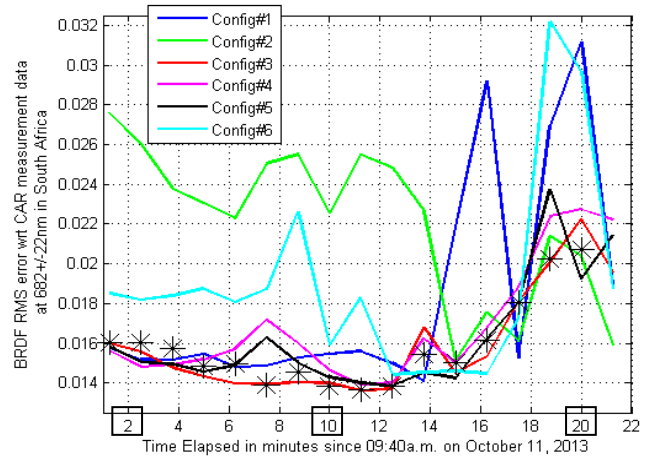


Figure 15: BRDF error over time as the 4 satellite cluster (different colors represent different architectures or configurations) flies over Southern Africa, assuming true BRDF to be as shown in Figure 3b all through. The black stars represent simulated BRDF errors by MISR (from TLE data), half an hour before in time. Measurement angles at the boxed times are shown in Figure 16.

Figure 16 shows the measurement angles sampled by Config #6, Config #3 and MISR for 3 instants of time (boxed in Figure 15) corresponding to medium, low and high errors. The intent is to identify the cluster orientations that caused the errors to change over time. Since Config #6 has only two different RAANs (Figure 14a), it is not able to cover both top and bottom hemispheres of the BRDF polar plot simultaneously – which was established as a chief error driver for vegetation in the previous section. 2-14 minutes after entering Africa, Config #6 shows relatively low errors because it samples the hotspot region however later the errors rise significantly because the samples rote to the anti hotspot hemisphere as seen in the first row of Figure 16. On the other hand, since Config #3 has three different RAANs (Figure 14b), it does a better job in at least partially covering both top and bottom hemispheres of the BRDF polar plot simultaneously as seen in the second row of Figure 16. It exhibits lowest errors between 2-12 minutes after entering Africa because it samples the hot spot and anti hotspot hemispheres, very close to their

exact positions on the BRDF polar plot. Later in time, the error rises slightly (not as much as Config #6) because the samples move out from near the hot spot but are still azimuthally spread

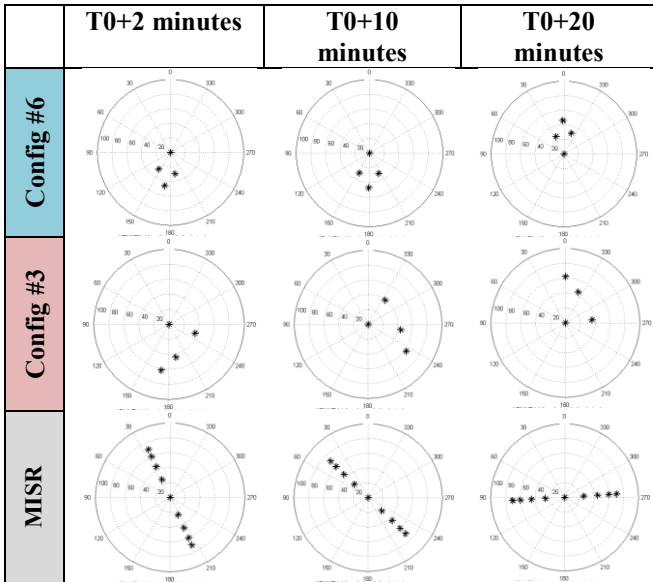


Figure 16: Sampling achieved of the BRDF polar plot for the best (Config #3) and worst (Config #6) configuration and MISR, as averaged over 22 minutes. T0 represents the time when the spacecraft (TERRA) or cluster each Southern Africa, subsequent times correspond to those boxed in Figure 15 and configurations (colors) correspond to Figure 15.

The rise of error with time for all configurations can be further avoided by placing additional satellites with *positive* true anomaly with respect to the reference satellite so that both hemispheres are covered at any given time. This option has not been studied or shown because it causes more differential drag, and in the absence of propulsion, increases the risk of inter-satellite collisions. MISR’s advantage in vegetation BRDF estimation is clearly deduced by comparing its configuration change (second row of Figure 16) and RMS error change (black asterisks in Figure 15) over time with the 4 satellite clusters in best or worst configuration. Since it samples the entire BRDF plot across in a straight line, it always covers both the hot spot *and* anti hotspot hemispheres and at a variety of view zenith angles to capture the hotspot irrespective of solar zenith angle. The only time the error rises slightly is when the samples are perpendicular to the principal plane (third row, third column in Figure 16). Nonetheless, cluster configurations have shown to produce errors equivalent to MISR therefore establishing their value in BRDF estimations.

5. CONCLUSIONS

We identify an important gap in the sampling abilities of earth observation missions –angular sampling – quantified by the BRDF metric and propose nanosatellite clusters in formation flight (FF) to make measurements to fill this gap.

In this paper, we demonstrated the science performance impact of such an approach using a comprehensive systems engineering model tightly coupled with a science evaluation model and tested it using state-of-the-art BRDF data collected during NASA’s airborne campaigns (heritage, golden standard). Both snow and vegetation environments were studied to understand the impact of biome selection of cluster designs. The BRDF model used to fit over the data was selected to be RLTS based on its heritage with snow and vegetation. Formation flight solutions in the linearized frames with and without perturbation forces and the global orbits frame using STK’s HPOP propagator were plugged into the model and compared with existing satellite solutions using their TLEs.

The coupled model was applied to different models and architectures of FF solutions, which simulated angular sampling, and used to calculate errors with respect to the golden standard. Specifically, four case studies were studied coupling different FF solutions with different biomes and applications (e.g, albedo). Insights on cluster design for BRDF learned from the case studies are presented and angular performance comparable to or better than current BRDF instruments demonstrated. Clusters can serve as a powerful complement to current flagship missions by providing 3D angular coverage of the Earth at acceptable signal to noise ratios such that their angular data products can be combined with the high quality images from the larger missions. As small satellite technologies for imaging and platform stability advance further, they are likely to become critical tools at reduced costs for a new paradigm in Earth Observation capability.

6. FUTURE WORK

There is much work to be done to evaluate the performance variation of FF clusters over time due to perturbation and other such effects (details of Box I in Figure 2). These are likely to cause performance degradation and will require precise maintenance maneuvers over time using an onboard propulsion

module. Trade studies of performance with respect to required delta-V as a function of the reference satellite's chief orbit and the cost of ground operations support form important considerations in the design of the cluster architectures, and will be studied. Global designs will also need to consider the biome spread of the Earth so that the clusters are in optimal configuration when they fly over the appropriate biomes. Finally, this work can be extended to calculate many geophysical parameters beyond snow albedo such as vegetation GPP and radiative forcing of clouds to demonstrate the impact of improved BRDF using clusters on critical science applications.

7. ACKNOWLEDGEMENTS

The authors are grateful to the following people for very useful discussions on the topics presented in this paper: Warren Wiscombe, Jacqueline LeMoigne, Alexis Lyapustin and Ralph Kahn from NASA GSFC, Marco Sabatini from Università degli Studi di Trento in Italy, David Miller from MIT and Thomas Hilker from Oregon State University.

REFERENCES

- [1] S. Nag and L. Summerer, "Behaviour based, autonomous and distributed scatter manoeuvres for satellite swarms," *Acta Astronaut.*, vol. 82, no. 1, pp. 95–109, Jan. 2013.
- [2] M. G. O'Neill, H. Yue, S. Nag, P. Grogan, and O. de Weck, "Comparing and Optimizing the DARPA System F6 Program Value-Centric Design Methodologies," in *Proceedings of the AIAA Space Conference*, Anaheim, California, 2010.
- [3] S. Nag, "Collaborative competition for crowdsourcing spaceflight software and STEM education using SPHERES Zero Robotics," Massachusetts Institute of Technology, 2012.
- [4] S. Nag, J. G. Katz, and A. Saenz-Otero, "Collaborative gaming and competition for CS-STEM education using SPHERES Zero Robotics," *Acta Astronaut.*, vol. 83, no. 0, pp. 145–174, Feb. 2013.
- [5] E. M. C. Kong and D. W. Miller, "Optimal spacecraft reorientation for earth orbiting clusters: applications to Techsat 21," *Acta Astronaut.*, vol. 53, no. 11, pp. 863–877, Dec. 2003.
- [6] S. Nag, "Design and Analysis of Distributed Nano-satellite systems for Multi-angular, Multi-spectral Earth Observation," in *Proceedings of the 64th International Astronautical Congress*, Beijing, China, 2013.
- [7] S. Nag, "Design of Nano-satellite Cluster Formations for Bi-Directional Reflectance Distribution Function (BRDF) Estimations," *AIAAUSU Conf. Small Satell.*, Aug. 2013.
- [8] D. J. Diner, J. C. Beckert, T. H. Reilly, C. J. Bruegge, J. E. Conel, R. A. Kahn, J. V. Martonchik, T. P. Ackerman, R. Davies, S. A. W. Gerstl, and others, "Multi-angle Imaging SpectroRadiometer (MISR) instrument description and experiment overview," *Geosci. Remote Sens. IEEE Trans. On*, vol. 36, no. 4, pp. 1072–1087, 1998.
- [9] X. Xiong, R. Wolfe, W. Barnes, B. Guenther, E. Vermote, N. Saleous, and V. Salomonson, "Terra and Aqua MODIS Design, Radiometry, and Geometry in Support of Land Remote Sensing," *Land Remote Sens. Glob. Environ. Change*, pp. 133–164, 2011.
- [10] J. Esper, S. Neeck, W. Wiscombe, M. Ryschkewitsch, and J. Andary, "Leonardo-BRDF: A New Generation Satellite Constellation," 2000.
- [11] L. Dyrud, J. Fentzke, G. Bust, B. Erlandson, S. Whitely, B. Bauer, S. Arnold, D. Selva, K. Cahoy, and R. Bishop, "GEOScan: A global, real-time geoscience facility," in *Aerospace Conference, 2013 IEEE*, 2013, pp. 1–13.
- [12] S. Nag and O. L. de Weck, "Tradespace Exploration of Distributed Nanosatellite Formations for BRDF Estimation," in *Proceedings of the International Workshop of Satellite Constellations and Formation Flying*, Lisbon, Portugal, 2013.
- [13] S. Nag, K. Cahoy, O. de Weck, C. Gatebe, B. Pasquale, G. Georgiev, T. Hewagama, and S. Aslam, "Evaluation of Hyperspectral Snapshot Imagers onboard Nanosatellite Clusters for Multi-Angular Remote Sensing," in *Proceedings of the AIAA Space Conference*, San Diego, 2013.
- [14] O. L. De Weck, U. Scialom, and A. Siddiqi, "Optimal reconfiguration of satellite constellations with the auction algorithm," *Acta Astronaut.*, vol. 62, no. 2, pp. 112–130, 2008.
- [15] S. Nag, J. A. Hoffman, and O. L. de Weck, "Collaborative and Educational Crowdsourcing of Spaceflight Software using SPHERES Zero Robotics," *Int. J. Space Technol. Manag. Innov. IJSTMI*, vol. 2, no. 2, pp. 1–23, 2012.
- [16] S. Nag, I. Heffan, A. Saenz-Otero, and M. Lydon, "SPHERES Zero Robotics software development: Lessons on crowdsourcing and collaborative competition," in *Aerospace Conference, 2012 IEEE*, 2012, pp. 1–17.
- [17] F. E. Nicodemus, *Geometrical considerations and nomenclature for reflectance*, vol. 160. US Department of Commerce, National Bureau of Standards Washington, D. C, 1977.
- [18] A. Lyapustin, C. K. Gatebe, R. Kahn, R. Brandt, J. Redemann, P. Russell, M. D. King, C. A. Pedersen, S. Gerland, and R. Poudyal, "Analysis of snow bidirectional reflectance from ARCTAS Spring-2008

- Campaign,” *Atmos Chem Phys*, vol. 10, no. 9, pp. 4359–4375, 2010.
- [19] S. Liang, *Advances in land remote sensing: System, modelling, inversion and application*. Springer, 2008.
- [20] J. L. Privette, T. F. Eck, and D. W. Deering, “Estimating spectral albedo and nadir reflectance through inversion of simple BRDF models with AVHRR/MODIS-like data,” *J. Geophys. Res.*, vol. 102, no. D24, pp. 29529–29, 1997.
- [21] C. K. Gatebe, “Airborne spectral measurements of surface–atmosphere anisotropy for several surfaces and ecosystems over southern Africa,” *J. Geophys. Res.*, vol. 108, no. D13, 2003.
- [22] C. K. Gatebe, E. Wilcox, R. Poudyal, and J. Wang, “Effects of ship wakes on ocean brightness and radiative forcing over ocean,” *Geophys. Res. Lett.*, vol. 38, no. 17, Sep. 2011.
- [23] B. A. Wielicki and E. F. Harrison, “Mission to planet Earth: Role of clouds and radiation in climate,” *Bull. Am. Meteorol. Soc.*, vol. 76, no. 11, 1995.
- [24] T. Hilker, N. C. Coops, F. G. Hall, C. J. Nichol, A. Lyapustin, T. A. Black, M. A. Wulder, R. Leuning, A. Barr, D. Y. Hollinger, B. Munger, and C. J. Tucker, “Inferring terrestrial photosynthetic light use efficiency of temperate ecosystems from space,” *J. Geophys. Res. Biogeosciences*, vol. 116, no. G3, p. n/a–n/a, 2011.
- [25] M. KING, M. STRANGE, P. Leone, and L. BLAINE, “Multiwavelength scanning radiometer for airborne measurements of scattered radiation within clouds,” *J. Atmospheric Ocean. Technol.*, vol. 3, pp. 513–522, 1986.
- [26] G. T. Georgiev, C. K. Gatebe, J. J. Butler, and M. D. King, “BRDF analysis of savanna vegetation and salt-pan samples,” *Geosci. Remote Sens. IEEE Trans. On*, vol. 47, no. 8, pp. 2546–2556, 2009.
- [27] M. O. Roman, C. K. Gatebe, Y. Shuai, Z. Wang, F. Gao, J. Masek, and C. B. Schaaf, “Use of In Situ and Airborne Multiangle Data to Assess MODIS- and Landsat-based Estimates of Surface Albedo,” 2012.
- [28] M. J. Barnsley, A. H. Strahler, K. P. Morris, and J. P. Muller, “Sampling the surface bidirectional reflectance distribution function (BRDF): 1. Evaluation of current and future satellite sensors,” *Remote Sens. Rev.*, vol. 8, no. 4, pp. 271–311, 1994.
- [29] T. Hilker, F. G. Hall, C. J. Tucker, N. C. Coops, T. A. Black, C. J. Nichol, P. J. Sellers, A. Barr, D. Y. Hollinger, and J. W. Munger, “Data assimilation of photosynthetic light-use efficiency using multi-angular satellite data: II Model implementation and validation,” *Remote Sens. Environ.*, vol. 121, pp. 287–300, 2012.
- [30] T. Hilker, N. C. Coops, F. G. Hall, T. A. Black, B. Chen, P. Krishnan, M. A. Wulder, P. J. Sellers, E. M. Middleton, and K. F. Huemmrich, “A modeling approach for upscaling gross ecosystem production to the landscape scale using remote sensing data,” *J. Geophys. Res. Biogeosciences 2005–2012*, vol. 113, no. G3, 2008.
- [31] J. R. Shell, “Bidirectional Reflectance: An Overview with Remote Sensing Applications & Measurement Recommendations,” *Rochester N. Y.*, 2004.
- [32] A. Ngan, F. Durand, and W. Matusik, “Experimental validation of analytical BRDF models,” in *ACM SIGGRAPH 2004 Sketches*, 2004, p. 90.
- [33] A. Ngan, F. Durand, and W. Matusik, “Experimental analysis of BRDF models,” in *Proceedings of the Sixteenth Eurographics conference on Rendering Techniques*, 2005, pp. 117–126.
- [34] A. Ngan, F. Durand, and W. Matusik, “Image-driven Navigation of Analytical BRDF Models,” in *Rendering Techniques*, 2006, pp. 399–407.
- [35] R. Latifovic, J. Cihlar, and J. Chen, “A comparison of BRDF models for the normalization of satellite optical data to a standard sun-target-sensor geometry,” *Geosci. Remote Sens. IEEE Trans. On*, vol. 41, no. 8, pp. 1889–1898, 2003.
- [36] F. Maignan, F.-M. Breon, and R. Lacaze, “Bidirectional reflectance of Earth targets: Evaluation of analytical models using a large set of spaceborne measurements with emphasis on the Hot Spot,” *Remote Sens. Environ.*, vol. 90, no. 2, pp. 210–220, 2004.
- [37] C. Schaaf, J. Martonchik, B. Pinty, Y. Govaerts, F. Gao, A. Lattanzio, J. Liu, A. Strahler, and M. Taberner, “Retrieval of Surface Albedo from Satellite Sensors,” in *Advances in Land Remote Sensing*, S. Liang, Ed. Springer Netherlands, 2008, pp. 219–243.
- [38] W. Wanner, X. Li, and A. H. Strahler, “On the derivation of kernels for kernel-driven models of bidirectional reflectance,” *J. Geophys. Res. Atmospheres*, vol. 100, no. D10, pp. 21077–21089, 1995.
- [39] H. Rahman, M. M. Verstraete, and B. Pinty, “Coupled surface-atmosphere reflectance (CSAR) model 1. Model description and inversion on synthetic data,” *J. Geophys. Res.*, vol. 98, no. D11, pp. 20779–20, 1993.
- [40] J. V. Martonchik, D. J. Diner, B. Pinty, M. M. Verstraete, R. B. Myneni, Y. Knyazikhin, and H. R. Gordon, “Determination of land and ocean reflective, radiative, and biophysical properties using multiangle imaging,” *Geosci. Remote Sens. IEEE Trans. On*, vol. 36, no. 4, pp. 1266–1281, 1998.
- [41] C. Cox and W. Munk, “Statistics of the sea surface derived from sun glitter,” *J Mar Res*, vol. 13, no. 2, pp. 198–227, 1954.
- [42] W. H. Clohessy, R.S. Wiltshire, “Terminal Guidance System for Satellite Rendezvous,” *J. Aerosp. Sci.*, vol. 27, pp. 653–658, 1960.
- [43] G. W. Hill, “Researches in the lunar theory,” *Am. J. Math.*, vol. 1, no. 1, pp. 5–26, 1878.
- [44] J. R. Wertz, *Orbit & Constellation Design & Management, second printing ed. El Segundo*. California: Microcosm Press, 2009.
- [45] S. A. Schweighart and R. J. Sedwick, “High-Fidelity Linearized J Model for Satellite Formation Flight,” *J.*

Guid. Control Dyn., vol. 25, no. 6, pp. 1073–1080, 2002.

- [46] M. Sabatini and G. B. Palmerini, “Linearized formation-flying dynamics in a perturbed orbital environment,” in *Aerospace Conference, 2008 IEEE*, 2008, pp. 1–13.
- [47] C. Sabol, C. McLaughlin, and K. Luu, “The Cluster Orbits With Perturbations of Keplerian Elements (COWPOKE) Equations,” DTIC Document, 2004.
- [48] S. Nag, J. LeMoigne, and O. L. De Weck, “Cost and Risk Analysis of Small Satellite Constellations for Earth Observation,” in *IEEE Xplore, Aerospace Conference 2014*, Big Sky, Montana, USA, 2014.
- [49] S. Nag, E. Gomez, S. Feller, J. Gibbs, and J. Hoffman, “Laser communication system design for the Google Lunar X-Prize,” in *Aerospace Conference, 2011 IEEE*, 2011, pp. 1–20.
- [50] R. Basri and D. W. Jacobs, “Lambertian reflectance and linear subspaces,” *Pattern Anal. Mach. Intell. IEEE Trans. On*, vol. 25, no. 2, pp. 218–233, 2003.
- [51] S. Nag, C. K. Gatebe, and O. L. De Weck, “Relative Trajectories for Multi-Angular Earth Observation using Science Performance Optimization,” *IEEE Aerosp. Conf. Proc.*, vol. accepted, Mar. 2014.

BIOGRAPHIES



Sreeja Nag is a PhD candidate in Space Systems Engineering at the Massachusetts Institute of Technology and a part-time research fellow at NASA Goddard Space Flight Center. She has a dual SM Candidate in Astronautics Engineering along with Technology & Policy at MIT. She has summer research experience with NASA JPL in 2008, the European Space Agency (ESTEC) in 2010 and led the SPHERES Zero Robotics Program in 2011. Email: sreeja_n@mit.edu



Charles Gatebe is a scientist with the Universities Space Research Association and the Principal Investigator of the Cloud Absorption Radiometer at NASA Goddard Space Flight Center. Email: Charles.K.Gatebe@nasa.gov



Olivier de Weck is a Professor of Aeronautics and Astronautics and Engineering Systems at the Massachusetts Institute of Technology. He is also the Executive Director of MIT Production in the Innovation Economy (PIE) Study and the Co-Director, Center for Complex Engineering Systems at KACST and MIT. Email: deweck@mit.edu